Can Cloud Images help in Predicting Geomagnetic Storms?

Rissnalin Syiemlieh[a], Eeshankur Saikia[a,**]

[a]Department of Applied Sciences, Gauhati University, Gopinath Bordoloi Nagar, Jalukbari, Guwahati, 781014, Assam, India

ARTICLE INFO

Keywords:
(Sun:) solar-terrestrial
Cosmic Rays
Geomagnetic indices
methods: data analysis
Wavelet Transformation
Fractal method.

ABSTRACT

Solar activity and Cosmic Ray particles are known to have an effect on the formation of structural clouds through changes in temperature. With an increase in solar activity, coronal mass ejection increases, leading to an increase in temperature in the Earth's atmosphere. The change in temperature is related to the change in cloud formation and rainfall distribution, and hence the change in climate pattern. This prompts us to analyse terrestrial cloud images for robust processing of underlying information or patterns. Geometrical exploration of cloud properties using Multi-Fractal Analysis (MFA) is given preference over standard statistical tools for devising an improved weather prediction platform in the future. For the first time, MFA is reported to be used successfully to analyse cloud properties using images obtained from satellites to predict geomagnetic storms.

1. Introduction

Strong Geomagnetic Storms (GMS) originate mostly due to Coronal Mass Ejection (CME) from the Sun and was found that 13 % is caused by Co-rotating Interaction Regions (CIR), the intense geomagnetic activity can also be due to fast streams of coronal holes (Srivastava and Venkatakrishnan (2004); Srivastava, Mathew, Louis and Wiegelmann (2009); Kilcik, Yigit, Yurchyshyn, Ozguc and Rozelot (2017)). CMEs launched from the Sun reach Earth's upper atmosphere in 1-5 days, depending on their speed (Webb, Cliver, Crooker, St Cyr and Thompson (2000); Srivastava and Venkatakrishnan (2004)). It is well known that CME creation is directly related to solar activity that increases or decreases with the solar cycle (Lean, Wang and Sheeley (2002); Yurchyshyn and Tripathi (2010); Tiwari, Pandey, Shrivstava and Srivastava (2011); Sharma, Srivastava, Chakrabarty, Moestl and Hu (2013); Mörner (2013)). Therefore, a link between solar activity and Earth's climate is well-known. Fallmann, Lewis, Castillo, Arnold and Ramsdale 2017 in their study found that the sea surface temperature affects the structure of the marine atmospheric boundary layer, which controls the exchange of heat and moisture between the ocean and the atmosphere, impacting the weather patterns. Their study confirms that when solar radiation is at its peak, the effect of the sea surface temperature forcing on cloud formation reaches its maximum. According to the Su and Kiang 2022 study, fluctuations in wind speed contribute to temperature changes in the terrestrial environment. Lower wind speed during the post-hiatus period results in warming, but higher wind speed during the hiatus period (a period of reduced global warming) is linked to cooling effects. They also pinpoint how cloud vertical structure is affected by temperature change, such that a lower cloud top height corresponds to warming during the post-hiatus period, and a greater cloud top height is linked to cooling effects during the hiatus period. Again, Liou and Ou 1989, in their research highlighted that cloud microphysical processes control the planet's energy balance. For instance, variations in cloud droplet concentrations and sizes can impact the amount of heat trapped in the atmosphere and the amount of Sunlight reflected into space. The temperature and climate of the globe are directly impacted by these variables. E. Palle Bago and C. J. Bulter established a link between Galactic Cosmic Rays (GCR), clouds factor and the Earth's climate. Their focus was on exploring the influences of the cosmic rays flux on clouds of different latitude zone of the Earth's atmosphere (Pallé Bagó and Butler (2000); Pallé and Butler (2002)). Their results show that the height of the clouds plays a role in understanding climate change (Pallé Bagó and Butler (2000)). Solar activity and cosmic rays in the terrestrial region are the characteristic conducts and factors with which an anomalous behaviour of GMS is explained.

Many researchers propose the prediction for space weather, involving the arrival time of the CME on the Earth's upper atmosphere and the corresponding magnitude of GMS. Such an attempt was made by Srivastava 2005b to predict GMS by identifying their source of origin and studying their behaviour for a better chance of forecasting GMS. Also, prediction using logarithmic relation is put forward by Srivastava 2005a for determining the behaviour of GMS. The Boller-Stolov model proposed that storms are controlled by the magnitude of the southward component of solar-magnetosphere wind (Boller and Stolov (1973); Russell and McPherron (1973)). Another model that focuses on the semi-annual variation, as the latitudinal variation of solar streams existed, this model postulated that the geomagnetic activity has two separations in annual variations with different phases due to the polarity of the interplanetary field (Russell and McPherron (1973)). The interplay between the upper atmosphere of the Earth and particles emanating due to CMEs from the Sun and GCR must play a role in the structural formation of clouds. The particles that carry the variability signature of the Sun and cosmic rays enter the Earth's atmosphere and interact with the magnetosphere, interfering with the path of the field lines and hence causing

**Corresponding author at Department of Applied Sciences, Gauhati University, Guwahati, 781014, Assam, India.
eeshankur@gauhati.ac.in. (E. Saikia)
ORCID(s):

a disturbance, which leads to GMS. Also, variability on the surfaces of the Sun introduces the Forbush effect on the GCR particles (Barouch and Burlaga (1975); Venkatesan and Ananth (1991); Cane (2000)).

Following the above understanding of GMS, we propose a new idea for predicting GMS by analysing the cloud images using the Multi-Fractal theory. Wavelet Transformation method (see Section 3) is used to study the interplay between the solar-terrestrial and cosmic-terrestrial, to provide evidence that climate change is due to their interaction. This change in climate affects cloud formation and thus influences rainfall distribution. Therefore, using the Multi-Fractal Analysis, we carried out a study using cloud images for GMS prediction. Multi-Fractal Analysis is a strong tool for the study of geometrical patterns formed as a result of nonlinear dynamical processes which is described in detail in Section 3, an observation of the results of both studies is discussed in Section 4 and lastly, a conclusion is drawn from our analysis in Section 5.

2. Data

Solar and Geomagnetic indices were retrieved from NASA archived (https://omniweb.gsfc.nasa.gov/form/dx1.html), the data on the website are combined data from Advance Composition Explorer (ACE), Wind Scapecraft, IMP 8 and Geotail, having data starting from 1-min time resolution. Cosmic rays data was retrieved from Sodankylä Geophysical Observatory (SGO) archived (http://www.sgo.fi/Data/archive.php). The neutron monitor (NM) in Oulu/SGO is one of the most stable and reliable stations of the World Neutron Monitor Network, it contains data starting from 1-min resolution (Usoskin, Mursula, Kangas and Gvozdevsky (2001)). NASA archived (https://data.giss.nasa.gov/gistemp/) also provide the combined data of surface temperatures for the Land-Surface Air and Sea-Surface Water Temperatures in terms of the global mean, the mean for the Northern Hemisphere, and the mean for the Southern Hemisphere with monthly resolution (Lenssen, Schmidt, Hansen, Menne, Persin, Ruedy and Zyss (2019); Team (2023)). Hence, monthly resolution data sets are considered as carried out for further analysis. De-trending of the time-series data is employed before the analysis is performed because of the observed trends in the time series. The cloud properties image data was retrieved from the Moderate Resolution Imaging Spectroradiometer (MODIS) data archive (https://modis.gsfc.nasa.gov/data/dataprod/mod06.php). The images measuring the cloud height from the top view were utilized for the Multi Fractal Analysis in the later part.

3. Methodology

3.1. Wavelet Transformation

As suggested by Torrence and Compo 1998 and Foufoula-Georgiou and Kumar 2014, a Wavelet Transformation (WT) is a signal transformation that incorporates time and frequency information of a signal without needing the signal to remain stationary. WT leverages the idea of breaking down a time-series signal and then precisely reconstructing it using the dilation and translation processes (Roesch, Schmidbauer and Roesch (2014); Schmidbauer and Roesch (2018)). The mother wavelet $\psi(t)$ uses the mathematical expression

$$\psi(t) = \pi^{-1/4} e^{i\omega t} e^{-t^2/2} \tag{1}$$

with angular frequency (ω) set to 6, since it makes the Morlet wavelet approximately analytic and is the preferred value in literature (Morlet, Arens, Fourgeau and Glard (1982b); Morlet, Arens, Fourgeau and Giard (1982a); Farge (1992); Roesch and Schmidbauer (2018)). WT can be a uni-variant wavelet transformation of a single time-series, it is known as Continuous Wavelet Transformation (CWT) whereas, a bi-variant wavelet transformation involving two time-series variables is called Cross Wavelet Transformation (XWT) (Liu (1994); Cazelles, Chavez, Berteaux, Ménard, Vik, Jenouvrier and Stenseth (2008); Aguiar, Soares et al. (2011)). The wavelets can be conveniently discretized in practical applications by setting dilation, $a = 2^s$ and translation, $b = \tau 2^s$ in octaves (Daubechies (1992)) to get

$$\hat{\psi}_{s\tau}(t) = 2^{-s/2}\psi(2^{-s}t - \tau) \tag{2}$$

where, s and τ are integers. Then, CWT is mathematically expressed as;

$$\hat{\psi}(s,\tau) = \frac{1}{\sqrt{2^s}} \int_{-\infty}^{+\infty} \psi(t)\psi^*(\frac{t}{2^s} - \tau)dt \tag{3}$$

and if $\psi_1(t)$ and $\psi_2(t)$ are the two time series simultaneously understudy, then XWT is given by,

$$W_{\psi_1\psi_2}(s,\tau) =< \hat{\psi_1}(s,\tau)\hat{\psi_2}^*(s,\tau) >= \left|W_{\psi_1\psi_2}(s,\tau)\right| e^{i\phi_i(s)} \tag{4}$$

where, phase $\phi_i(s)$ describes the delay between the two signals variable at time t_i on a scale s. Details of this transformation can be seen in (Maraun and Kurths (2004); Schmidbauer and Roesch (2018)). Wavelet analysis of the speed of Solar Wind (SW) particles, Cosmic Rays (CR) particles, terrestrial Geomagnetism indicators (ap-index), and combined terrestrial Surface temperatures are studied to provide needed evidence for solar-terrestrial and cosmic-terrestrial interaction which are the main cause of climate change on the Earth's atmosphere.

3.2. Fractal Theory

Benoit B. Mandelbrot was the first to introduce the application of fractal analysis to natural time series data (Mandelbrot and Mandelbrot (1982)) and later Multi-Fractal method was used for the study of turbulence which was further used by many mathematicians and physicists for their studies (Véhel and Vojak (1995); Jaffard (1997)). The MFA was used in a seismic study to determine the complexity of fractals using the Multi-Fractal parameters (Telesca, Lapenna and Macchiato (2004)). The fractal community also recommends Multi-Fractal studies for image analysis. A fractal dimension that is important for characterising the image in terms of its fractal structure can be computed from an image that represents the critical state of a specific process (Vehel and Mignot (1994); Lopes and Betrouni (2009)).

3.2.1. Box Dimension

This dimension implements the box-counting method to estimate the fractal dimension by using a least-squares fitting. It is known for its simplicity of measuring the fractal dimension (D) of a signal/ data. The principles involved in estimating the dimension of image data are simply covering the grayscale image with cubes of width ϵ, the D is mathematically defined as;

$$D = \lim_{\epsilon \to 0} \frac{log N(\epsilon)}{log(1/\epsilon)} \tag{5}$$

where $N(\epsilon)$ is the number of smallest cubes of width ϵ required to cover over an image. The slope of an ordinary least squares linear fitting estimates the required dimension (Hall and Wood (1993); Davies and Hall (1999); Gneiting, Ševčíková and Percival (2012)). This method is acknowledged to have limitations because it is the simplest way to measure the fractal dimension. We introduce the Multi-Fractal study, which is recognised as the most significant fractal estimation, in order to be precise and thorough.

3.2.2. Multi-Fractal Approach

This method considers a multiscale image, let's say $a(x, t)$, where t is a time parameter measuring the little information that filters out from an image and furthermore takes into consideration the global information (Lévy-Véhel (1998)). Scaling analysis is therefore related to t because it also evaluates the size of the neighbourhood, which affects the value of $a(t)$ at x (Lévy-Véhel (1998)). In order to directly extract information from singularities, this Image Multiscale Analysis (IMA) employs scale invariant and translation concepts. The points that make up the structural (edge) information in the images are thought to have regularities that differ from the background regularity of the original image. Without making any assumptions about its regularity or structure, this approach is used (Lévy-Véhel (1998)). The structure of singular measures can also be found in MFA (Hentschel and Procaccia (1983); Holley and Waymire (1992)), which is also used to measure robustness, such as that of Choquet capacities (Véhel and Vojak (1998)). It is renowned for measuring unique instances of self-affinity and resemblance in both deterministic and unpredictable situations (Falconer (1994); Arbeiter and Patzschke (1996)). Lévy-Véhel 1998 provides a detailed explanation of the Multi-Fractal principle for image analysis. The point-wise structure of a singular measure is analysed through a spectrum called the Multi-Fractal spectrum.

3.2.3. Multi-Fractal spectrum

The spectrum known as the Multi-Fractal spectrum gives either geometrical or probabilistic information about the distribution of points that have the same singularity. Multi-Fractal spectrum satisfies the Hölder spectrum formalism, which interns depend on Hölder regularity(α). The parameter mainly depends on the statistical approaches or theories used for a given set of functions (Jaffard (1997); Véhel (2002)). Some research has shown that the Multi-Fractal spectrum is an adequate measure for geometrical structure or fractal pattern (Harrar and Khider (2014)). The Multi-Fractal technique of the probabilistic approach of the scale was used to probe some intrinsic features present in stereometric images (Stach, Roskosz, Cwajna and Cybo (2006)). Multi-Fractal methods have drawn attention to analysing singular signals, both for theory and application (Véhel and Guilheneuf (1997)).

Considering a distribution measured by μ (multiplicative construction of the density) in space, the probability of a point belonging to a set. The density distribution of this set will fail if the distribution is found to be singular. The strength of the singularities of μ is measured by exponent $\alpha(x)$ called Hölder exponent, which distinguishes the Multi-Fractals. K_α which describes the points of equal strength lying on interwoven fractal sets;

$$K_\alpha = \left| x \epsilon \mathbb{R}^d \, : \, \alpha(x) = \lim_{B \to (x)} \frac{\log \mu(B)}{\log |B|} \right| \tag{6}$$

where B is a ball containing x with its diameter $|B|$ tending to zero. Hausdorff dimension measures the size of the fractal sets K_α to identify the geometry of the singular distribution μ as (Riedi (1999); Zeković and Reljin (2014)),

$$f_H(\alpha) = dim(K_\alpha) \tag{7}$$

A continuous spectrum of $f_H(\alpha)$ Vs α known as the Hausdorff spectrum or Singularity spectrum uses the exponent α to describe the erratic dynamics of the Multi-Fractal system in terms of value and shape. The α measures the signal's regularity and is presented to detect the discontinuity that occurs in a dynamic signal. These discontinuities in a signal are located when the number of continuous derivatives of the signals, where the Hölder exponent changes, become significant (Riedi (1999)). Therefore, the spectrum measures the degree of the nonlinearity in irregular signals (Zeković and Reljin (2014)). Yalamova 2006 stated that MFA amplifies the non-linear geometrical pattern in the time series and in estimating the Hausdorff dimension. Xu, Ji and Fermüller 2009 uses the Multi-Fractal formalism in characterising the different types of patterns which give rise to the spatial distribution of pixels in an image. The MFA was used in a seismic study to determine the complexity of fractals using the Multi-Fractal parameters, Hölder exponent α (Telesca et al. (2004)).

The Hausdorff spectrum is obtained from step-wise functionality operation. Firstly, de-noising and normalization of the data, and checking the noise level in a function will determine the nuisance factor needed to be eliminated, hence smoothing the signals. Secondly, the function is detrended or decomposed where fractal behaviour is observed, called singularities (Donoho (1995); Véhel and Guilheneuf (1997); Véhel (2002)). Here, the Hausdorff spectrum is used to identify the nonlinear dynamics in the cloud properties for earlier detection of terrestrial weather changes, yielding storms, or sub-storm. The Multi-Fractal parameter, i.e., Hölder exponent observed from our analysis is important as it explained the enhancement of fractal structure. When we observed a α with high value, the geometrical abundance is in higher scale or self-similar fractal information appeared in a large area. And if an observed α value is low, the self-similar structural enrichment appeared in a small area.

We have adopted this methodology to analyse the satellite images of the cloud for the robust pattern shown by them. This study can contribute to differentiating the pattern seen in the analysed cloud data, which can provide insight into the GMS prediction. There are different methods with which this spectrum can be generated, since our is an image (2-D) data, we have adopted the segmentation method following the theory presented above.

4. Results and Discussion

4.1. Wavelet Analysis

CWTs are used for analysing the time series of the mean Surface Temperature (in Global, Northern Hemisphere, and Southern Hemisphere) of the Earth's atmosphere (i.e., the combined surface temperature of Land, Sea, and Air), the speed of the SW particles which originates from solar activity (CMEs), the galactic cosmic ray in the heliosphere which is modulated by the solar magnetic activity and lastly the Geomagnetic Indices (GMI) in terms of ap-index which describe the global variation of magnetic activity of the Earth due to the solar phenomena.

4.1.1. Continuous Wavelet Analysis

CWT and its Average powers use the intrinsic signal to modulate the intrinsic signature of the time series with 95% significant inside the Cone Of Influence (COF) marked by the black line inside the white contour of the wavelet plot (Roesch and Schmidbauer (2018)). The Average wavelet power shows the variation of the most significant period over the average wavelet power of the time series. Various periods' modulation of 95% significant is shown by the CWTs of the time-series understudy, such as the 1-year period of the Earth's revolution around the Sun. The $\sim$ 1.7 year period which is the quasi-periodicity of cosmic variation, is known to be the period of combined action of the large solar events (CMEs) and long-lived Global Merged Interaction Regions (that is, $\sim$ 1 year recovery time of cosmic ray intensity at 1 AU) (Kato (2003)). The periods $\sim$ 3.8 and the $\sim$ 8 years period also called the oction and octoeteris are due to the lunar cyclic changes in the climatic characteristic and are the manifestation of the El Niño Southern Oscillation (ENSO) and North Atlantic Oscillation (NAO) (Pozo-Vázquez, Esteban-Parra, Rodrigo and Castro-Díez (2001); Wilson (2012); Sidorenkov (2016)). The distribution of rainfall in the Pacific Ocean's tropical zone is known to be directly impacted by ENSO, which is a

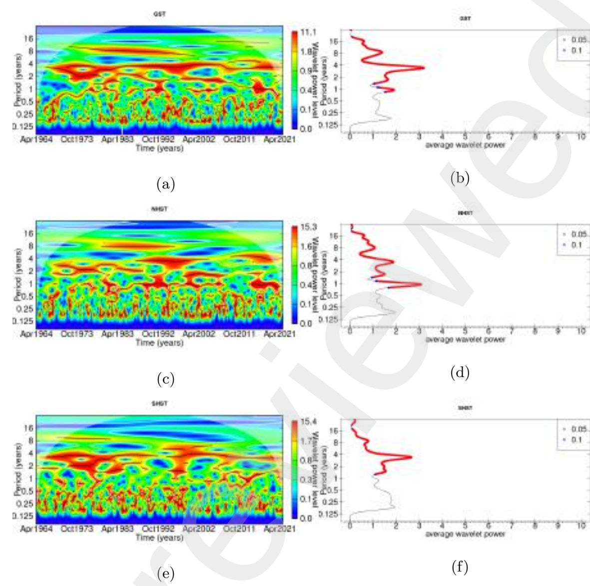

Figure 1: The plots describe the CWT (left) and its Average wavelet power (right) of the time-series: where (a) & (b) is for Global Surface Temperature, (c) & (d) is for Northern Hemisphere Surface Temperature, and (e) & (f) for Southern Hemisphere Surface Temperature. The black line inside the white contour expressed the 95% significant period over a timescale in the CWT, and the periods plotted in the Average wavelet power (marked with red dots) exhibit 95% significant.

temporal variation in the central and eastern Pacific Ocean and the difference in sea level pressure between subpolar and subtropical latitudes is the NAO. The periods 2.33 and 4.66 years are the periodic wind variation in the equatorial stratosphere called the Quasi-Biennial Oscillation (QBO), which results from the downward propagation of easterlies and westerlies wind (Reed (1965b,a); Lindzen and Holton (1968); Baldwin, Gray, Dunkerton, Hamilton, Haynes, Randel, Holton, Alexander, Hirota, Horinouchi, Jones, Kinnersley, Marquardt, Sato and Takahashi (2001)). Lastly, the Sun's solar cycle period, which is the 11 year period (Vines (2008); Hathaway (2015); Mironova, Aplin, Arnold, Bazilevskaya, Harrison, Krivolutsky, Nicoll, Rozanov, Turunen and Usoskin (2015)) is also observed from the CWTs and its Averages.

Figure 1, shows the CWT and its Average power plots of the time series of Global Surface Temperature (GST), Northern Hemisphere Surface Temperature (NHST), and Southern Hemisphere Surface Temperature (SHST) of the Earth's atmosphere. The above mention periods are observed in the sub-figures of Figure 1. A maximum amplitude significant period of $\sim$ 3.8 years are seen in sub-figures 1 (b) and (f) for GST and SHST time-series, but this period even though significant does not have a maximum amplitude in NHST time-series and is suppressed by the 1-year period of maximum amplitude (refer sub-figures 1 (d)). The significant $\sim$ 1.7 and 11 years period are also observed in the CWT of

GST, NHST, and SHST time-series as shown in Figures 1 (b), (d) and (f) respectively.

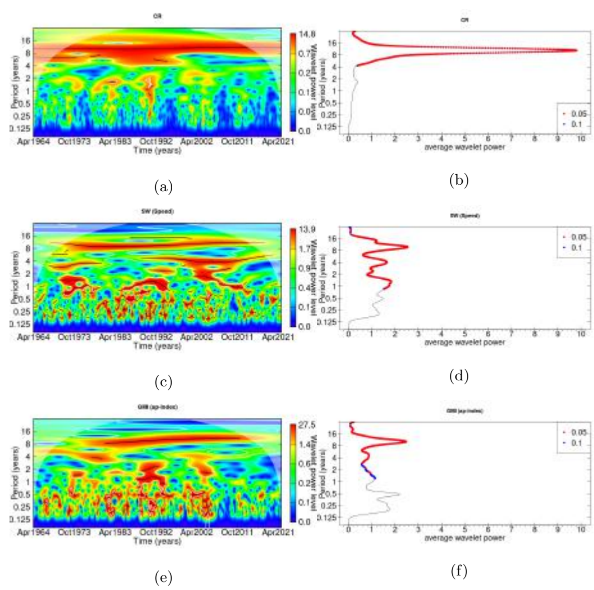

Figure 2: Plots describes: (a), (b) are the CWT and Average wavelet power of the Cosmic Rays; (c), (d) are the CWT and Average wavelet power of the Solar Wind particles speed; and (e), (f) is the CWT and Average wavelet power of the Geomagnetic indices (ap-index).

Again, Figures 2 show the CWT and its Average power plots of the time series of Cosmic Rays (CR), SW particle Speed, and GMI (ap-index). In this figure, the significant period modulation of 11 years has a maximum amplitude and is the most dominating period throughout the CR time series (refer to sub-figures 2 (a) and (b)). Although, the ∼ 1.7 year period shows up in CWT of CR, but is not consistent throughout the timescale (refer to sub-figures 2 (a)). The 11 year's significant period of maximum power shows up in both the SW (speed) and GMI (ap-index) time-series throughout the timescale of the CWT plots (refer Figure 2 (c), (d), (e) and (f)). After the 11 year period, ∼ 4 and ∼ 1.7 years significant period are seen to have the second-highest amplitude of the average power, followed by 1 and 2.33 years period in the Average wavelet power plot of SW particles speed time-series (refer to sub-figure 2 (d)). Similarly, ∼ 4 and ∼ 1.7 years significant period are also observed in the CWT and the Average wavelet power plots of the GMI (ap-index) time-series (refer to sub-figure 2 (f)). These significant periods observed in their individual intrinsic signals will play a role in their interaction, which is further discussed in the next section.

4.1.2. Cross Wavelet Analysis

The cross wavelet transformation (XWT) is used to study the interplay between two time series in terms of their periodic interaction, which are constructive (in-phase) that intensify their average power and are destructive (out-of-phase) which subside their average power. From this analysis four plots are observed, they are the XWT plot which describes the wavelet phase interaction (black arrows) of the periodic variation (i.e, the periods are of 95% significant inside the white contour region with black arrows (resultant phase direction) observed in XWT), the Average XWT plot shows the average wavelet power coefficient Vs periods observed with significant of 95% (that is, red dots in the average wavelet power plot), the Coherence XWT plots which show the constructive interaction of the observed period with power bar significant and its Average Coherence plot which shows the significant period's interaction Vs coefficient of the average coherence.

The XWT plots between GST, NHST, and SHST with CR time series are shown in Figure 3. From the XWT and Average XWT plots of GST Vs CR and NHST Vs CR time-series, significant periodic variation of similar amplitude with maximum average power for the 11 year period followed by ∼ 3.8 and ∼ 1.7 year period of lesser amplitude are observed (refer sub-figures 3 (a), (b) and sub-figures 3 (e), (f) for GST VS CR and NHST Vs CR respectively). Also, its Coherence and its Average Coherence plots show the highest correlation interaction for the significant 11 year period (maximum amplitude) with coefficient value ≥ 0.55 and a significant 0.5 year period (which is the half revolution period of the Earth around the Sun) with ≥ 0.1 coefficient value. Although the same periodic variation is seen in the XWT and its Average XWT of SHST Vs CR time-series, the constructive interaction seen from their Coherence and Average Coherence does not show up with high significance except for 11 year period having 90% significant (blue dots in the average coherence plot) and coefficient value of 0.4 (refer to sub-figures 3 (i), (j), (k) and (l)). This may be due to the tilt in the Earth's axis which causes a non-uniform solar and cosmic radiation to reach the terrestrial environment, hence explaining the periodic variation in the Southern Hemisphere region.

Again, checking the XWT plots of the time series between GST, NHST, and SHST with SW particle speed is shown in Figure 4. The XWT and its Average power of GST vs SW particle speed time-series show a correlation interaction period which is of 95% significant having maximum amplitude at 11 and ∼ 3.8 years followed by lesser amplitude periods of 1 and ∼ 1.7 years (refer to sub-figures 4 (a) and (b)). The Coherence and its Average Coherence coefficient show effective cross-correlation interaction with 95% significant for 8 − 16 years and 4.66 year periods, and with 90% significant for 1 year period (refer to sub-figures 4 (c) and (d)). Also, the XWT and its Average power of NHST vs SW particle speed time-series describe the significant period of maximum amplitude at 11 year followed by lesser amplitude periods of 1, ∼ 3.8, ∼ 1.7 years respectively (refer sub-figures 4 (e) and (f)). The Coherence interaction between NHST vs SW particle speed is given in sub-figures 4 (g)

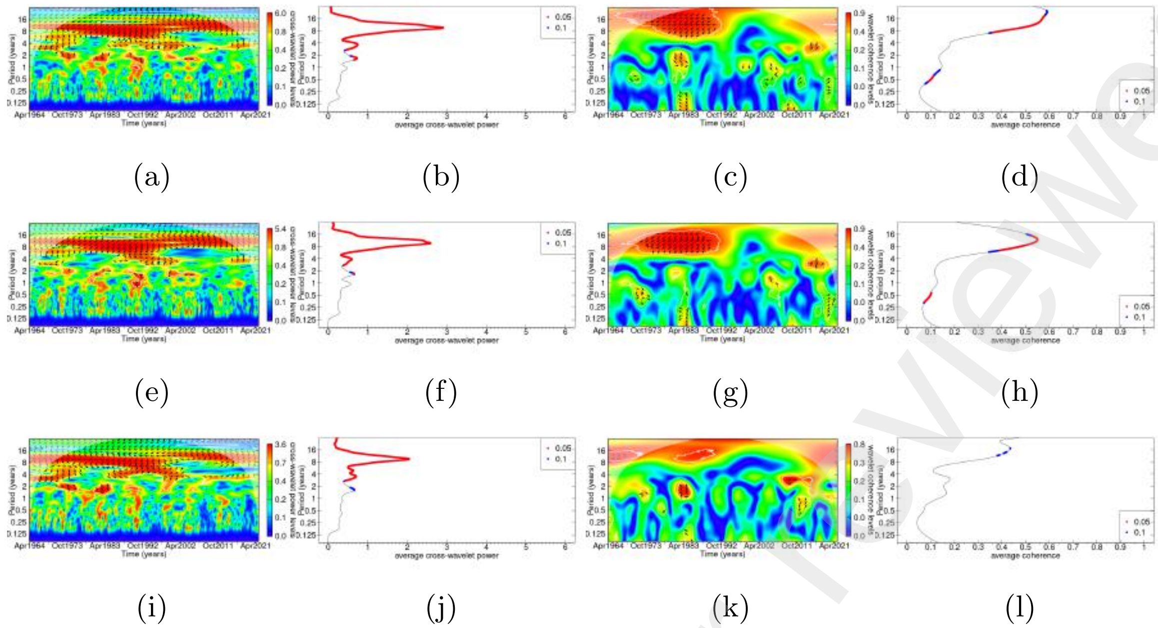

Figure 3: The Plots describe the cross-correlations plots of Surface Temperature (Global, Northern Hemisphere, and Southern Hemisphere) and Cosmic Rays, where (a), (b), (c) & (d) are the XWT, the average cross-wavelet power, the Coherence, and the Average Coherence coefficient of the Global Surface Temperature with Cosmic rays; similarly, (e), (f), (g) & (h) are the XWT, the average cross-wavelet power, the Coherence, and the Average Coherence coefficient of the Northern Hemisphere Surface Temperature with Cosmic Rays; and lastly, (i), (j), (k) & (l) as the XWT, the average cross-wavelet power, the Coherence, and the Average Coherence coefficient between Southern Hemisphere Surface Temperature and Cosmic Rays.

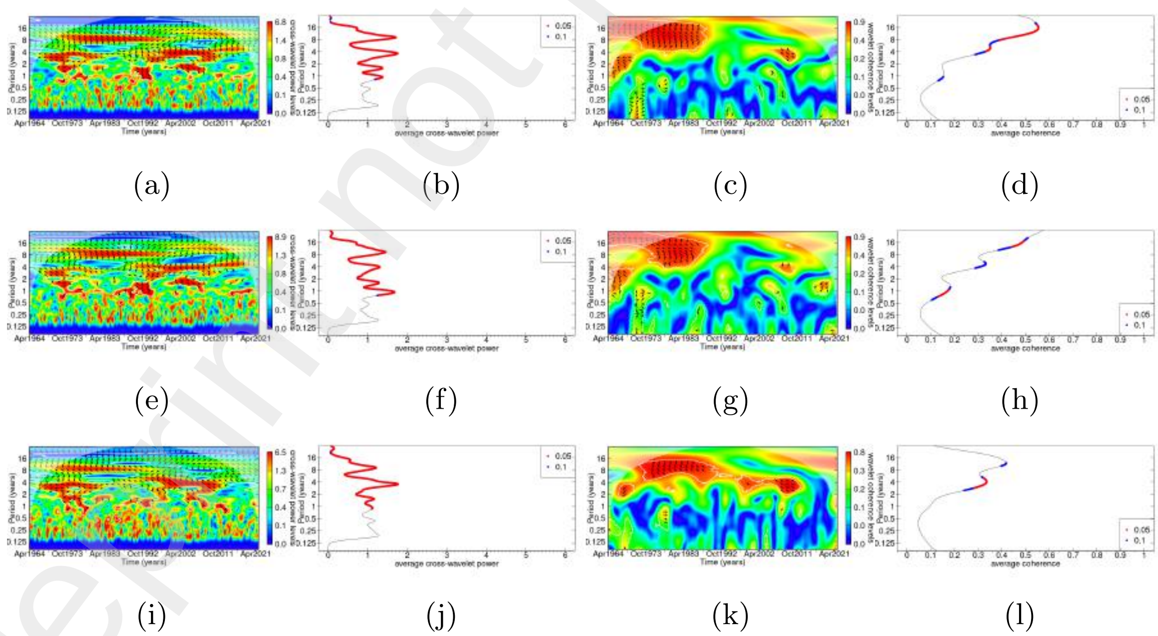

Figure 4: Here; (a), (b), (c) & (d) are the XWT, the Average XWT, the Coherence, and the Average Coherence between Global Surface Temperature with Solar Wind particles speed. (e)- the XWT, (f)-the Average XWT, (g)- the Coherence & (h) the Average Coherence between Northern Hemisphere Surface Temperature and Solar Wind particles speed. And (i), (j), (k) & (l) describes the XWT, the Average XWT, the Coherence, and the Average Coherence between Southern Hemisphere Surface Temperature and Solar Wind particles speed respectively.

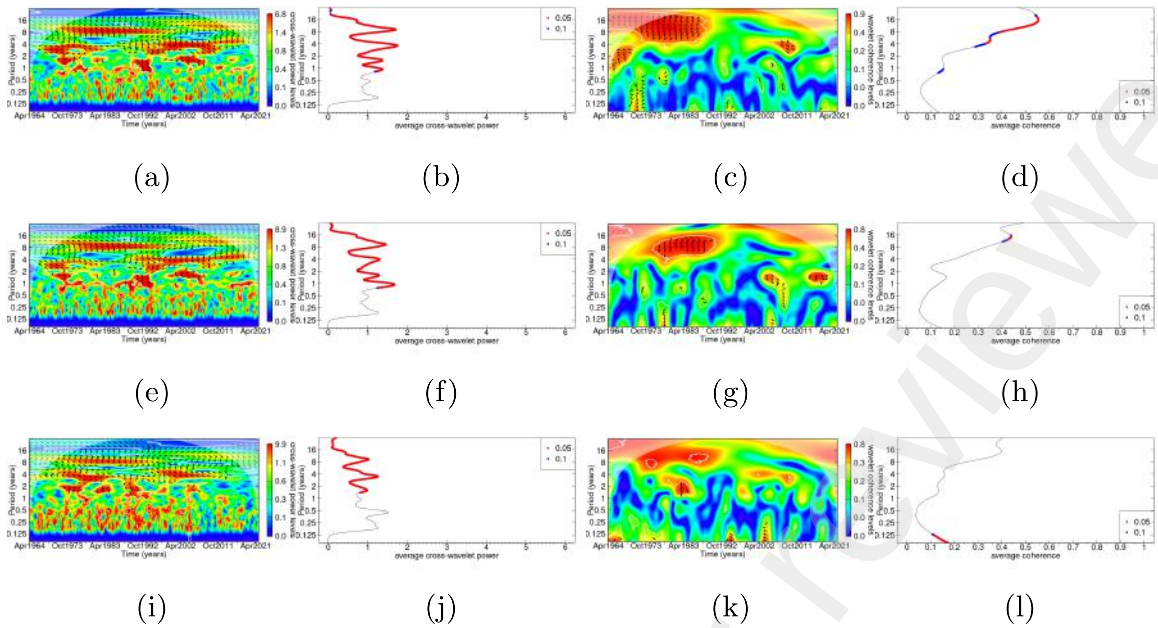

Figure 5: The plots show the XWT as (a), the Average XWT as (b), the Coherence as (c) & the Average Coherence as (d) between Global Surface Temperature and Geomagnetic indices (ap-index). Similarly, (e), (f), (g) & (h) are it's the XWT, Average XWT, Coherence, and Average Coherence coefficient between Northern Hemisphere Surface Temperature and Geomagnetic indices (ap-index). Lastly, (i), (j), (k) & (l) are the XWT, the Average XWT, the Coherence, and the Average Coherence coefficient of Southern Hemisphere Surface Temperature and Geomagnetic indices (ap-index) time series.

and (h). Here, the 7 − 14 years and 1 year have the highest significance, followed by the ∼ 4 year period with 90% significant. Again, the XWT and its Average power of the time-series SHST and SW particle speed shows the significant period of ∼ 3.8 year to have the maximum amplitude other than the 11, ∼ 1.7 and 1 years period respectively (refer sub-figures 4 (i) and (j)). Only the ∼ 4 year period (with 95% significant) is sustained in the cross-correlation interaction between the SHST and SW particle speed, shown by its Coherence and Average Coherence plots (refer to sub-figures 4 (k) and (l)). The 11 year period is observed to have constructive interaction with 90% significant (refer to sub-figures 4 (k) and (l)).

The cross-correlation interaction of the surface temperature of the Global, Northern, and Southern hemispheres with magnetic disturbances in the terrestrial region is given in Figure 5. First, the XWT and its Average power plots of GST, NHST, and SHST with ap-index of GMI, show a similar pattern to that of XWT and its Average power plots of GST, NHST, and SHST with SW particle speed (refer Figure 5). This is expected, as the ap-index measures the magnetic fluctuation resulting from the solar activity interaction with the magnetosphere in the terrestrial region. The Coherence and its Average Coherence plots on the contrary differ for the NHST, SHST with GMI(ap-index) when compared to NHST, SHST with SW particle speed (refer sub-figures 5 (a)-(j)). Only the 11 year period is observed to be the most significant period of interaction between NHST and GMI(ap-index) (refer to sub-figures 5 (g) and (h)). But, SHST and GMI(ap-index) shows inconsistent interaction for ∼ 1.7 year period over the timescale in the Coherence plot and hence are not significant in the Average Coherence plot (refer sub-figures 5 (k) and (l)).

Lastly, the cross-correlation plots for the SW particles speed, CR with ap-index of GMI is presented in Figure 6. In this figure, the XWT and its Average power plots of SW particles speed with ap-index of GMI, shows the maximum amplitude at 11 year period and lesser amplitude periods of ∼ 1.7, ∼ 4 and 2.33 years (with 95% significant) respectively in sub-figures 6 (a), (b). Again, the XWT and its Average power plots of CR with ap-index of GMI give the significant 11 year period of maximum amplitude and the subsided 4.66 year significant period (refer to sub-figures 6 (e), (f)). The cross-correlated coherence between the SW particle speed, CR, and GMI (ap-index), shown in sub-figures 6 (c), (d) and sub-figures 6 (g), (h) respectively indicate the significant periods of 11 year (maximum coefficient) to be the main period for their interplay. The 11 year period shows a 0.8 average coherence coefficient for solar particles and 0.7 average coherence coefficient for cosmic particles when interacting with terrestrial magnetic properties, implying that solar particles colliding on the Earth magneto-shield is higher in comparison to the cosmic ray particles, it may be due to the higher number of constituents particles entering the atmosphere.

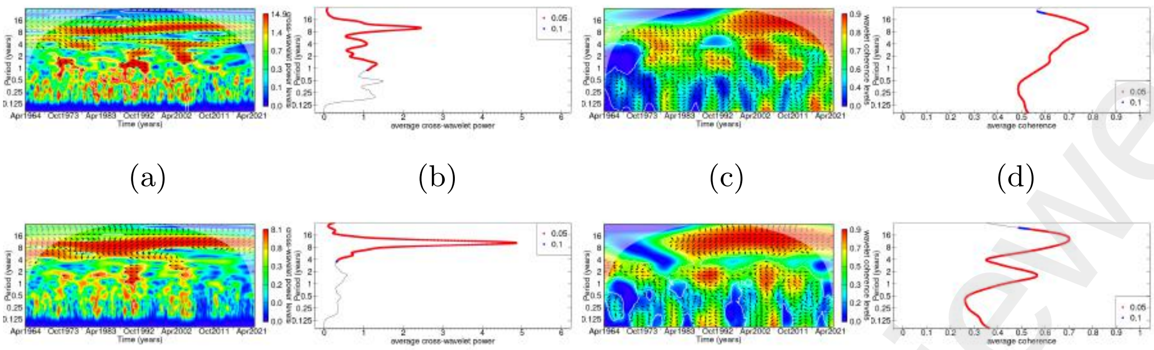

(a) (b) (c) (d)

(e) (f) (g) (h)

Figure 6: The plots describe (a), (b), (c) & (d) as the XWT, the Average XWT, the Coherence and the Average Coherence of cross-correlated Solar Wind particles Speed and Geomagnetic indices (ap-index) time-series. And (e), (f), (g) & (h) are the XWT, the Average XWT, the Coherence, and the Average Coherence plots cross-correlated of Cosmic rays and Geomagnetic indices (ap-index) time series.

4.1.3. Phase Coherence Analysis

In the Wavelet Coherence plots of the cross-correlated time series of mean Surface temperature, SW particle speed, CR, and GMI (ap-index), the direction of phase angle (black arrows) indicates the phase difference (phase lag) between the two time series (refer to sub-figures 3-5(c), (g), (k)). It is possible to determine which time series is more influential than another based on the phase lag (Roesch and Schmidbauer (2018)). Thus, the phase difference between the two time series interprets the act with which one causes the effect observed on the other. From the phase difference, we estimate the time delay, as described by Assous and Linnett 2012 and Cao and Wang, 2022. The estimated time lag from the phase difference is shown in Tables 1-3.

From Table 1, the time lags between the GST, NHST and SHST with CR of the cross-correlated Coherence period are mostly influenced by the Solar-Lunar cycle and their interplay. Corresponding periods of 0.375-,0.437-, 0.475-, 0.64-, 0.85- year are multiple of Solar and Lunar Cycle of ∼ 27 days (Wilson (2012); Katsavrias, Hillaris and Preka-Papadema (2016); Sidorenkov (2016)). The time lags of 3.8-, 5-, 5.5-, 6.87- years are the period manifestation of ENSO and the 3.8-, 8-, 10- year are the signature period of seasonal lunar tides cycle (Munnich, Cane and Zebiak (1991); Lachniet, Burns, Piperno, Asmerom, Polyak, Moy and Christenson (2004); Wilson (2012); Katsavrias et al. (2016); Sidorenkov (2016)). Again, in Table 2, the time lags observed between GST, NHST, SHST, and SW shows the signature of both the lunar and solar cycle (periods less than 1 year). The periods of ≤2, 3-, 4.1- year are bearing the signature of ENSO and 1.74 year is the period of NAO which happens to also be the cosmic variation period with solar magnetic activity (Schneider and Schönwiese (1989); Kato (2003)). The time lag of 1.16 years happens to be the period of QBO (Mukherjee, Indira, Reddy and BV (1985)). From Table 3, the time lags observed from the Coherence plots of GST, NHST, and SHST with GMI(ap-index) indicate the lunisolar interaction of 0.64-, 0.87- (multiple of a 27-day cycle). The time lag of 1.74-year along with 1-, 1.06-, 1.27-, 1.5-, 2-, 2.75-, 4-, 6- years are thought to be manifestations of QBO, ENSO, and NAO. These time-lags indicates the influence of the Solar-Moon-Earth interaction system along with effects from other climate change pattern such as ENSO, QBO, and NAO. Solar-Cosmic-Terrestrial interaction seems to be the cause and effect of the majority of the variations, leaving an indication of the influence of Solar-Cosmic interactions on climate change.

The wavelet analysis concludes that the terrestrial surface temperature is influenced by solar activity, cosmic rays particles, and lunar cycles. The periods 11 and ∼ 1.7 years, which measured the solar activity of the solar cycle and varying cosmic rays intensity in the terrestrial region are observed from the Coherence analysis of SW, CR with surface temperature. The other cross-correlation periods of ∼ 1.7, ∼ 3.8, 4.66/2.33, and $8-16$ years seen from the CR, SW particles speed interplay with surface temperature explains the climate pattern manifestation of QBO, ENSO, and NAO. Therefore, the interaction of the solar-terrestrial, cosmic-terrestrial, and lunar cycles is the sole reason why the climate pattern in the Earth's atmosphere changes.

4.2. Fractal and Multi-Fractal Analysis

The interaction of solar-terrestrial, and galactic-terrestrial led to structural cloud formation in the Earth's atmosphere (Todd and Kniveton (2001); Sun and Bradley (2002); Usoskin and Kovaltsov (2008); de Wit and Watermann (2010); Yurchyshyn and Tripathi (2010); Tiwari et al. (2011); Mörner (2013)). Cloud formation in the coastal region is more sensitive to the variation of terrestrial atmosphere (Schwartz, Gershunov, Iacobellis and Cayan (2014)), an example during Oct 17^{th}-23^{rd}, 1999, at the Chilean coast showed structural formation on the cloud, prompted us to go for the MFA of

Table 1
An estimated phase lag and time lag from Cross Wavelet Coherence of mean Surface temperature (GST, NHST, and SHST) and CR is given below:

Cross Coherence time-series	Period (years)	Phase lag (radian)	Time lag (years)	Refer
GST Vs CR	∼ 1.7	$\frac{3\pi}{4}$	0.64	Figure 3 (c), (d)
	∼ 3.8	$\frac{\pi}{4}$	0.475	
	∼ 8	$\frac{5\pi}{4}$	5	
	∼ 11	π	5.5	
	∼ 16	$\frac{5\pi}{4}$	10	
NHST Vs CR	∼ 0.5	$\frac{7\pi}{4}$, $\frac{3\pi}{2}$	0.437, 0.375	Figure 3 (g), (h)
	∼ 1.7	$\frac{3\pi}{4}$, π	0.64, 0.85	
	∼ 3.8	$\frac{\pi}{4}$	0.475	
	∼ 8	$\frac{5\pi}{4}$	5	
	∼ 11	π, $\frac{5\pi}{4}$	5.5, 6.87	
	∼ 16	π	8	
SHST Vs CR	∼ 1.7	$\frac{3\pi}{4}$	0.64	Figure 3 (k), (l)
	∼ 3.8	2π	3.8	

the cloud formation images before the geomagnetic storm, which occurred during Oct 21^{st} - 22^{nd}, 1999 (Basu, Basu, Valladares, Yeh, Su, MacKenzie, Sultan, Aarons, Rich, Doherty et al. (2001)), to see if the storm prediction could have been possible.

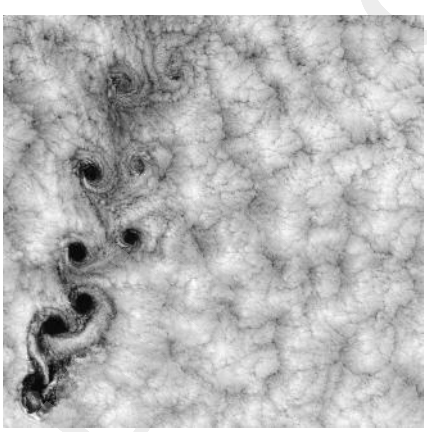

Figure 7: The cloud formation during Oct $17^{th} - 23^{rd}$,1999, collected from NOAA (NCEI).

Figure 7, was collected and processed by IBTrACS, University of North Carolina at Asheville, from the National Oceanic and Atmospheric Administration (NOAA), National Centers for Environmental Information (NCEI) in Asheville, NC (http://www.atms.unca.edu/ibtracs/index.shtml). Since then, a well-known influence of Earth's climate was established with cosmic rays and solar activity (Pallé Bagó and Butler (2000); Pallé and Butler (2002)). This means that solar and cosmic interaction in the terrestrial region will affect cloud structural formation. It is seen that high solar activity results in a decrease in cooling clouds (low-height clouds), which led to a global increase in radiating transfer (temperature) (Pallé Bagó and Butler (2000)). The height of clouds is linked to their thickness which interlinks to the interaction of particles, and hence pertaining information of the surrounding atmosphere. Therefore, analysing cloud properties should reveal the underlying pattern of their particle interaction and should support an idea for predicting geomagnetic storms.

Egyptian and Japanese Station observed a disorder or fluctuation in the atmosphere of the Earth with the formation of a cloud swirling structure during the mid of February 2014 and March 2015. In the same region where spinning cloud structures were observed soon before the GMS event occurs. There was a GMS during February 18^{th}, 20^{th}, 23^{rd} and 27^{th} of 2014 in Egypt and March 17^{th}-18^{th} of 2015 in Japan (Ghamry, Lethy, Arafa-Hamed and Abd Elaal (2016); Marubashi, Cho, Kim, Park, Ishibashi et al. (2016)), falling on the descending phase (high CME events or solar activity) of the solar cycle. Hence, cloud image data is chosen to analyse and tally, focusing on Egypt and Japan region. The mean value of the Cloud Top Height is measured by NASA

Table 2
This table reports the inferences drawn from Cross Wavelet Coherence of mean Surface temperature (GST, NHST, and SHST) and SW particle speed.

Cross Coherence time-series	Period (years)	Phase lag (radian)	Time lag (years)	Refer
GST Vs SW	~ 1	$\frac{\pi}{2}$	0.25	Figure 4 (c), (d)
	~ 1.7	$\frac{3\pi}{4}$	0.637	
	~ 2.33	π	1.165	
	~ 3.8	$\frac{3\pi}{4}$	1.425	
	~ 4.66	$\frac{\pi}{4}, \frac{\pi}{2}$	0.58, 1.165	
	~ 8	$\frac{3\pi}{4}$	3	
	~ 11	$\frac{3\pi}{4}$	4.13	
	~ 16	$\frac{\pi}{2}$	4	
NHST Vs SW	~ 1.7	$\frac{\pi}{4}, \frac{5\pi}{4}$	0.213, 1.06	Figure 4 (g), (h)
	~ 2.33	$\frac{3\pi}{4}$	0.87	
	~ 4.66	$\frac{\pi}{2}, \frac{3\pi}{4}$	1.165, 1.747	
	~ 11	$\frac{3\pi}{4}$	4.125	
SHST Vs SW	~ 2.33	$\frac{5\pi}{4}$	1.456	Figure 4 (k), (l)
	~ 4	$\frac{3\pi}{4}$	1.5	
	~ 11	$\frac{3\pi}{4}, \frac{\pi}{4}$	4.125, 1.375	

(National Aeronautics and Space Administration) instruments, MODIS, and is collected as used in our analysis. The parameter is found to be the most suitable for our purpose since it contains the effect of convection in transferring radiated energy while forming the cloud volume.

Cloud has two main roles having opposite effects, they act as a cooler by reflecting solar radiation and warmer by trapping the radiation emitted from Earth's surfaces (Pallé Bagó and Butler (2000)). As the cloud reflects radiation, the radiation transfer must be less in that area where the formation of the cloud is observed. A prominent decrease in the radiated transfer is observed during 17^{th}, 18^{th} and 27^{th} February 2014 with decreasing Mean Top Cloud Height parameter in the Egypt region of Figure 8 which must lead to the formation of swirling clouds just before GMS. First, the estimated fractal dimension using the box-counting method for the cloud images understudy is examined. The fractal dimension estimated for these images was found to be greater than 2 shown in Table 4. This suggests an abundance of fractal attributes or structures in an image is present above 2 or from 2 onwards. This is important because the enhancement or changes in the structure or fractal attribute which is observed in the Hausdorff dimension are found to be around this dimension. Table 4 also shows that during the occurrence of GMS on 18^{th}, 23^{rd} and 27^{th} February 2014, the box dimension is lesser when compared to the earlier day. The outcome of using the Multi-Fractal approach to the cloud images is the individual Hausdorff spectrum or spectra per day. Figure 9 shows the Hausdorff spectra of the Mean Cloud Top Height images, which are analysed using MFA. Hausdorff Spectra of the Cloud images are found to be a reliable tool for predicting a storm by observing the α parameter of the spectra of days before an event. Two inferences can be drawn from these spectra, first, the sharp peaks become more prominent and amplitude increases before the GMS event and second, there is a shifting of the Hölder exponent from small α to large α or large α to small α in reference to the peak observes, before the GMS event. Now, keeping the two inferences in mind, Figure 9 is checked more clearly. From the Spectra, we observed a variation or shift in the α value along the axis (for e.g., the shift of α from $\alpha = 2.25$ to $\alpha = 2.6$ and again to $\alpha = 2.25$ as observed from sub-figures 9 (a), (b) and (c) respectively) corresponding to the Sharpe peak annotated with red rectangle covering the peak considered. This observation of a shift in Hölder exponent corresponds to cloud images of 15^{th}, 16^{th} and 17^{th} February 2014 which is before the storms occurred, that is, the 18^{th} February 2014. Also, the exponent of the reference peak on the 18^{th} February 2014 is shifted to larger α and the peak is not prominent in its amplitude, this may be explained

Table 3
Describe the phase lag and time lag estimated from Cross Wavelet Coherence of mean Surface temperature (GST, NHST and SHST) and GMI (ap-index).

Cross Coherence time-series	Period (years)	Phase lag (radian)	Time lag (years)	Refer
GST Vs ap-index	~ 1.7	$\frac{3\pi}{4}$	0.64	Figure 5 (c), (d)
	~ 2.33	$\frac{3\pi}{4}$	0.874	
	~ 3	π	1.5	
	~ 4.66	$\frac{3\pi}{4}$	1.74	
	~ 8	$\frac{\pi}{2}$, $\frac{\pi}{4}$	2, 1	
	~ 11	$\frac{3\pi}{4}$	4.125	
	~ 16	$\frac{\pi}{2}$, $\frac{3\pi}{4}$	4, 6	
NHST Vs ap-index	~ 1.7	$\frac{5\pi}{4}$, $\frac{7\pi}{4}$	1.06, 1.5	Figure 5 (g), (h)
	~ 11	$\frac{\pi}{2}$	2.75	
SHST Vs ap-index	~ 1.7	$\frac{3\pi}{2}$	1.275	Figure 5 (k), (l)

Table 4
Box Dimension (D) of Mean Cloud Top Height property from 15^{th}-27^{th} Feb 2014

Date	D
15-02-2014	2.1655
16-02-2014	2.1632
17-02-2014	2.165
18-02-2014	2.1629
19-02-2014	2.1605
20-02-2014	2.163
21-02-2014	2.1638
22-02-2014	2.1636
23-02-2014	2.1589
24-02-2014	2.1613
25-02-2014	2.1631
26-02-2014	2.1713
27-02-2014	2.1643

Table 5
Box Dimension (D) of Mean Cloud Top Height property from 13^{th}-18^{th} March 2015

Date	D
13-03-2015	2.1633
14-03-2015	2.1678
15-03-2015	2.1695
16-03-2015	2.1673
17-03-2015	2.1654
18-03-2015	2.1628

by the GMS that occurred during this day. The 19^{th} and 20^{th} February 2014 which refer to sub-figures 9 (e) and (f) shows an increase in the amplitude of the Sharpe peak at $\alpha = 2.5$ when the storm occurred. Again, from sub-figures 9 (g), (h), and (i), we observe a slight shift of the reference peak to the left of $\alpha = 2.5$ in sub-figure 9 (g), again to the right in sub-figure 9(h) and completely disappear on the GMS day, that is sub-figure 9 (h). Lastly, sub-figures 9 (j) and (k) show the peak at $\alpha = 2.3$ becomes more prominent from its previous day and a shift of this peak to a higher exponent is seen in sub-figures 9 (k). And lastly, an increase of the amplitude of the Sharpe peak at $\alpha = 2.7$ and $\alpha = 3.1$ during the 27^{th} day, which happens to be the GSM event day. These observations from the Hausdorff spectrum of the cloud paint a picture or pattern for identifying the GMS events before their occurrence and hence leads to at least 1-3 day prior prediction. Now, we will see if this holds well for a different storm in another location of the Earth, i.e., GMS occurred during March 17^{th} and 18^{th}, 2015 in Japan region. Table 5 shows the decrease of the dimension of the cloud images during the occurrence of GMS events in comparison to those before the event. Figure 10 shows the Mean Top Cloud Height images which are to be analysed for storms that occurred in Japan region. We observed the radiated transfer in Japan region to decrease from 15^{th}-18^{th}, in March 2015 which stated a change in terms of cloud structure. The Hausdorff Spectra of the cloud images shown in Figure 11 clearly, show the variation of the reference peak across the Hölder exponent i.e, α value, during 13^{th}, 14^{th}, 15^{th} March 2015 (refer sub-figures 11 (a), (b) and (c)), which may be a lead for the occurrence of GMS on 17^{th} and 18^{th} March 2015 in the Japan region. Also, sub-figure 11 (d) shows a decrease in the amplitude of the reference peak at $\alpha = 2.25$ prior to the GMS event. Hence, the Hausdorff spectrum of the Mean Top Cloud Height exhibits a pattern of shift and amplification of the reference peaks in the Hölder exponent one–three days before an actual storm event.

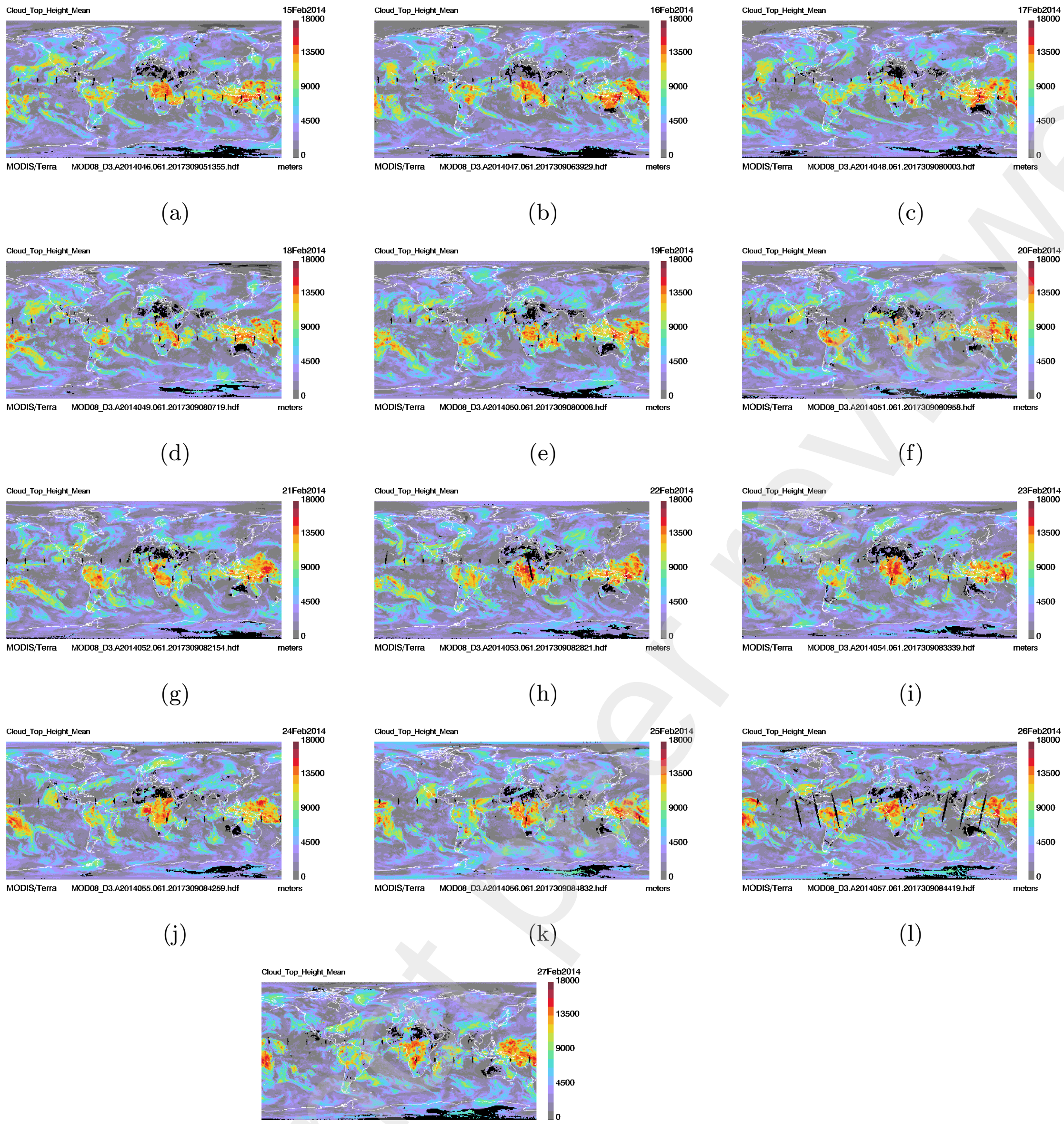

(a) (b) (c) (d) (e) (f) (g) (h) (i) (j) (k) (l) (m)

Figure 8: The Mean Cloud Top Height images from 15^{th} February to 27^{th} February 2014. The Cloud in Egypt region during 17^{th}, 25^{th} and 27^{th} February 2014 was seen to have a lesser height in comparison with others. The Top Height on 15^{th}, $18^{th}-19^{th}$, $20^{th}-21^{st}$, and $25^{th}-26^{th}$ February 2014 may be seen to be anomalous in comparison to that on other days.

5. Conclusion

The change in solar and cosmic radiation is the main cause of the temperature change in the terrestrial environment which are linked to climate change pattern. In this paper, we study the periodic interaction of the solar-terrestrial and cosmic-terrestrial, to find evidence of their role in this interplay. Their cross-correlation analysis has shown that the solar cycle period is the most significant period that dominates this interplay. Moreover, we have observed that the periods which demonstrate the climate change pattern such as ENSO, QBO, and NOA in the Earth's atmosphere also exist. It is known that temperature variation is the sole reason that affects the formation of clouds and thus, rainfall distribution on the planet. Therefore, we have proposed a new idea for analysing cloud images for geomagnetic storm prediction. Besides, it is observed for the first time, on the basis of our results obtained from the MFA of the terrestrial cloud images that the tools available in MFA may be used reliably to predict geomagnetic storms at least one-three days before the occurrence of the event.

Acknowledgement

In order to complete this research, the authors thank NASA, SGO, and MODIS repositories/archives for making

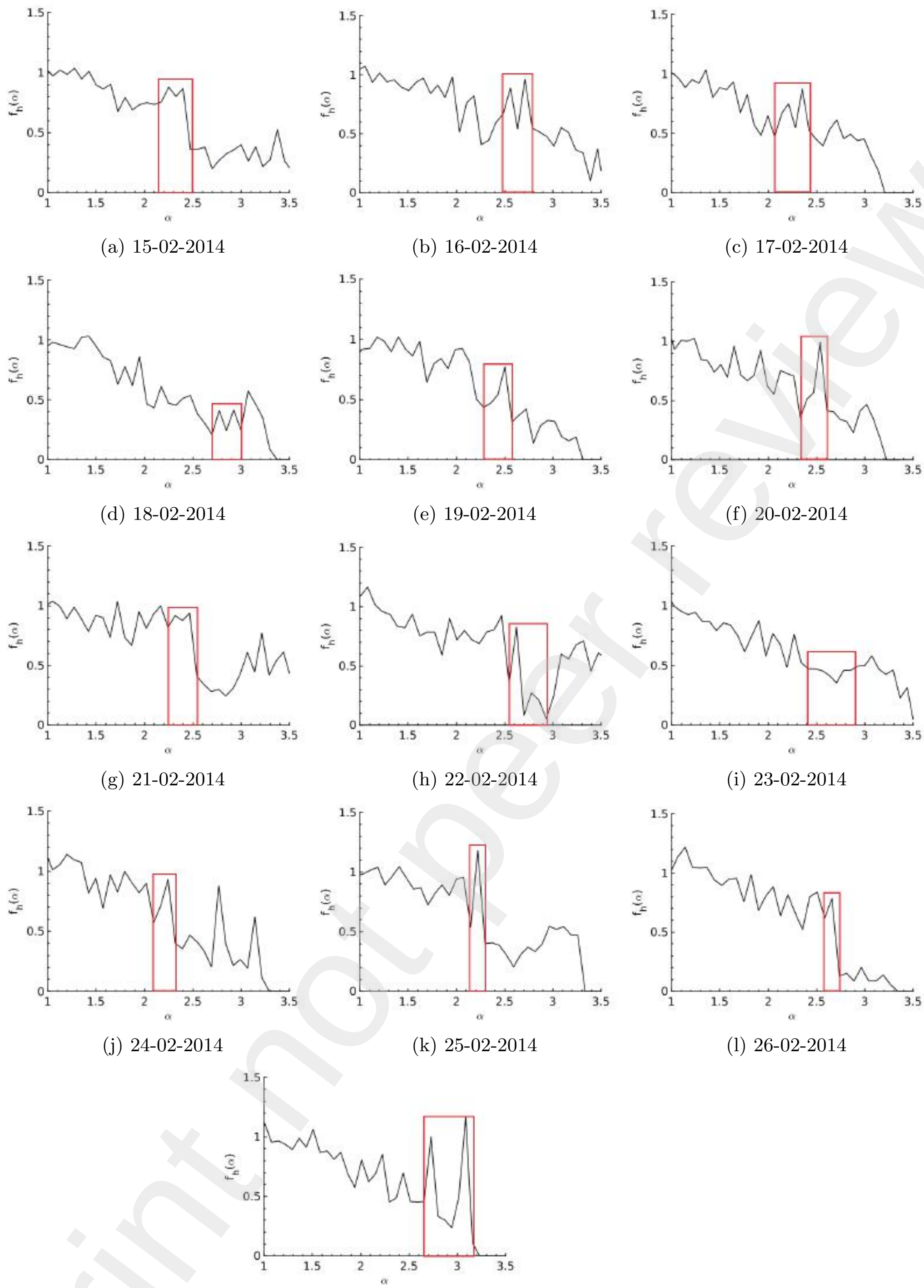

(a) 15-02-2014 (b) 16-02-2014 (c) 17-02-2014

(d) 18-02-2014 (e) 19-02-2014 (f) 20-02-2014

(g) 21-02-2014 (h) 22-02-2014 (i) 23-02-2014

(j) 24-02-2014 (k) 25-02-2014 (l) 26-02-2014

(m) 27-02-2014

Figure 9: The Hausdorff Spectra of Mean Cloud Top Height images from 15^{th} February to 27^{th} February 2014. Onset of storms on $18^{th}, 20^{th}, 23^{rd}$ and 27^{th} could be predicted from the anomalous spectrum peak on $15^{th} - 16^{th}, 19^{th} - 20^{th}, 21^{st} - 22^{nd}$ and 25^{th}.

necessary data publicly available (see Section-2 for further information on the data sources). We appreciate Joe King and Natalia Papitashvili of NASA/SPDF for making the OMNI 2 data and the public database of the OMNIWeb service available at https://omniweb.gsfc.nasa.gov/ow.html. The cloud data can be found at https://modis.gsfc.nasa.gov/data/dataprod/mod06.php. We also thank Steve Platnick and Steve Ackerman for making it available. Also for the cosmic data as http://www.sgo.fi/Data/archive.php provided by the cosmic rays group associated with the Space Physics and Astronomy Research Unit and Sodankylä Geophysical Observatory.

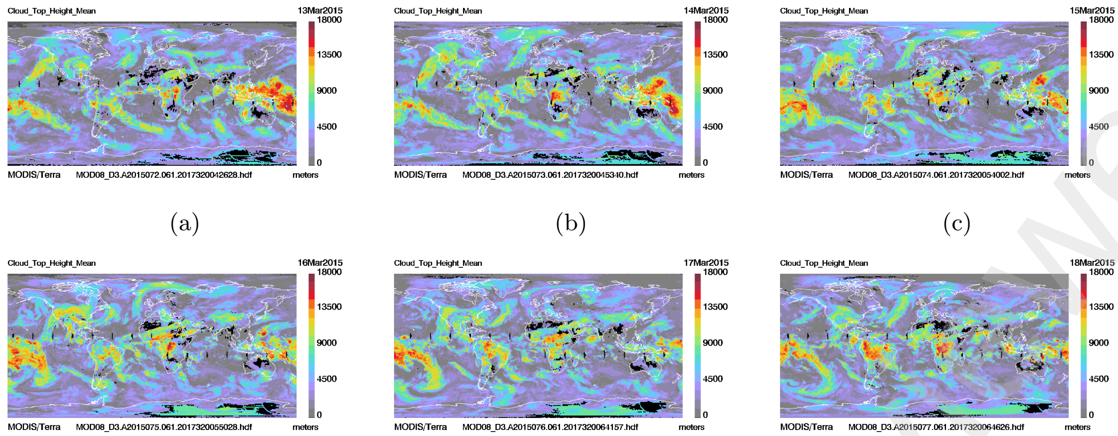

(a) (b) (c)

(d) (e) (f)

Figure 10: The Mean Cloud Top Height images from 13^{th} March to 18^{th} March 2015. The Clouds height in Japan region from 14^{th}-18^{th} March 2015 is seen to be lesser in comparison to other days.

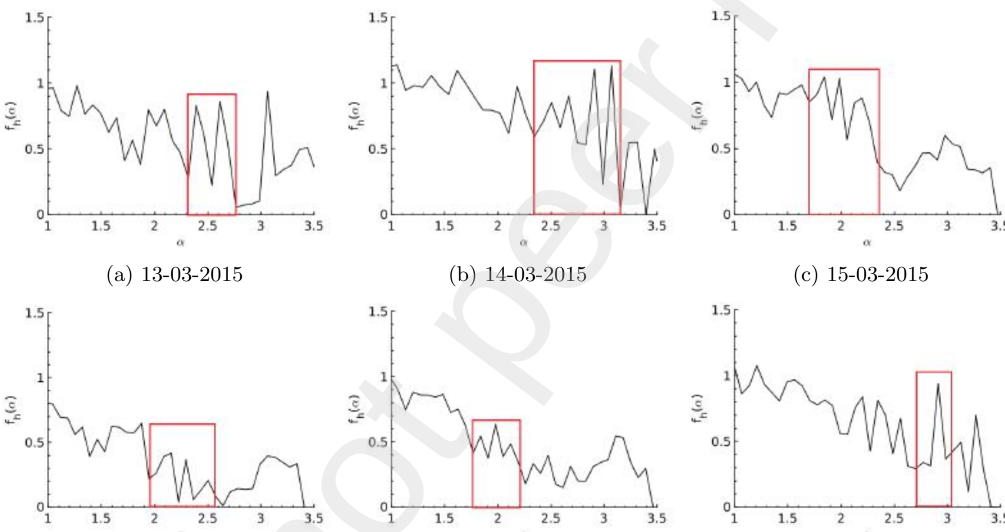

(a) 13-03-2015 (b) 14-03-2015 (c) 15-03-2015

(d) 16-03-2015 (e) 17-03-2015 (f) 18-03-2015

Figure 11: The Hausdorff Spectra of Mean Cloud Top Height images from 13^{th} March to 18^{th} March 2015. Onset of storms on 17^{th} and 18^{th} could have been predicted from the anomalous Spectrum peak on 14^{th}, 15^{th} and 16^{th}.

References

Aguiar, L.F., Soares, M.J., et al., 2011. The continuous wavelet transform: A primer. Technical Report. NIPE-Universidade do Minho.

Arbeiter, M., Patzschke, N., 1996. Random self-similar multifractals. Mathematische Nachrichten 181, 5–42.

Assous, S., Linnett, L., 2012. High resolution time delay estimation using sliding discrete fourier transform. Digital Signal Processing 22, 820–827. URL: https://www.sciencedirect.com/science/article/pii/S1051200412001078, doi:https://doi.org/10.1016/j.dsp.2012.05.001.

Baldwin, M.P., Gray, L.J., Dunkerton, T.J., Hamilton, K., Haynes, P.H., Randel, W.J., Holton, J.R., Alexander, M.J., Hirota, I., Horinouchi, T., Jones, D.B.A., Kinnersley, J.S., Marquardt, C., Sato, K., Takahashi, M., 2001. The quasi-biennial oscillation. Reviews of Geophysics 39, 179–229. URL: http://doi.wiley.com/10.1029/1999RG000073, doi:10.1029/1999RG000073.

Barouch, E., Burlaga, L., 1975. Causes of forbush decreases and other cosmic ray variations. Journal of Geophysical Research 80, 449–456.

Basu, S., Basu, S., Valladares, C., Yeh, H.C., Su, S.Y., MacKenzie, E., Sultan, P., Aarons, J., Rich, F., Doherty, P., et al., 2001. Ionospheric effects of major magnetic storms during the international space weather period of september and october 1999: Gps observations, vhf/uhf scintillations, and in situ density structures at middle and equatorial latitudes. Journal of Geophysical Research: Space Physics 106, 30389–30413.

Boller, B.R., Stolov, H.L., 1973. Explorer 18 study of the stability of the magnetopause using a kelvin-helmholtz instability criterion. Journal of Geophysical Research 78, 8078–8086.

Cane, H.V., 2000. Coronal mass ejections and forbush decreases, in: Cosmic Rays and Earth. Springer, pp. 55–77.

Cao, Z., Wang, T., 2022. Water-temperature controlled deformation patterns in heifangtai loess terraces revealed by wavelet analysis of insar time series and hydrological parameters. Frontiers in Environmental Science , 1515.

Cazelles, B., Chavez, M., Berteaux, D., Ménard, F., Vik, J.O., Jenouvrier, S., Stenseth, N.C., 2008. Wavelet analysis of ecological time series. Oecologia 156, 287–304.

Daubechies, I., 1992. Ten lectures on wavelets: Society for industrial and applied mathematics. Philadelphia, Pennsylvania .

Davies, S., Hall, P., 1999. Fractal analysis of surface roughness by using spatial data. Journal of the Royal Statistical Society: Series B (Statistical Methodology) 61, 3–37.

Donoho, D.L., 1995. De-noising by soft-thresholding. IEEE transactions on information theory 41, 613–627.

Falconer, K.J., 1994. The multifractal spectrum of statistically self-similar measures. Journal of theoretical Probability 7, 681–702.

Fallmann, J., Lewis, H., Castillo, J.M., Arnold, A., Ramsdale, S., 2017. Impact of sea surface temperature on stratiform cloud formation over the north sea. Geophysical Research Letters 44, 4296–4303.

Farge, M., 1992. Wavelet transforms and their applications to turbulence. Annual review of fluid mechanics 24, 395–458. doi:10.1146/annurev.fl.24.010192.002143.

Foufoula-Georgiou, E., Kumar, P., 2014. Wavelets in geophysics. volume 4. Elsevier.

Ghamry, E., Lethy, A., Arafa-Hamed, T., Abd Elaal, E., 2016. A comprehensive analysis of the geomagnetic storms occurred during 18 february and 2 march 2014. NRIAG Journal of Astronomy and Geophysics 5.

Gneiting, T., Ševčíková, H., Percival, D.B., 2012. Estimators of fractal dimension: Assessing the roughness of time series and spatial data. Statistical Science , 247–277.

Hall, P., Wood, A., 1993. On the performance of box-counting estimators of fractal dimension. Biometrika 80, 246–251. URL: https://doi.org/10.1093/biomet/80.1.246, doi:10.1093/biomet/80.1.246, arXiv:https://academic.oup.com/biomet/article-pdf/80/1/246/616276/80-1-246.pdf.

Harrar, K., Khider, M., 2014. Texture analysis using multifractal spectrum. International Journal of Modeling and Optimization 4, 336.

Hathaway, D.H., 2015. The Solar Cycle. Living Reviews in Solar Physics 12, 4. URL: http://www.ncbi.nlm.nih.gov/pubmed/27194958, doi:10.1007/lrsp-2015-4.

Hentschel, H.G.E., Procaccia, I., 1983. The infinite number of generalized dimensions of fractals and strange attractors. Physica D: Nonlinear Phenomena 8, 435–444.

Holley, R., Waymire, E.C., 1992. Multifractal dimensions and scaling exponents for strongly bounded random cascades. The Annals of Applied Probability , 819–845.

Jaffard, S., 1997. Multifractal formalism for functions part i: results valid for all functions. SIAM Journal on Mathematical Analysis 28, 944–970.

Kato, C., 2003. A ∼1.7-year quasi-periodicity in cosmic ray intensity variation observed in the outer heliosphere. Journal of Geophysical Research 108, 1367. doi:10.1029/2003JA009897.

Katsavrias, C., Hillaris, A., Preka-Papadema, P., 2016. A wavelet based approach to Solar–Terrestrial Coupling. Advances in Space Research 57, 2234–2244. URL: http://dx.doi.org/10.1016/j.asr.2016.03.001, doi:10.1016/j.asr.2016.03.001.

Kilcik, A., Yigit, E., Yurchyshyn, V., Ozguc, A., Rozelot, J., 2017. Solar and geomagnetic activity relation for the last two solar cycles. Sun and Geosphere 12, 31–39.

Lachniet, M.S., Burns, S.J., Piperno, D.R., Asmerom, Y., Polyak, V.J., Moy, C.M., Christenson, K., 2004. A 1500-year el niño/southern oscillation and rainfall history for the isthmus of panama from speleothem calcite. Journal of Geophysical Research: Atmospheres 109.

Lean, J.L., Wang, Y.M., Sheeley, N.R., 2002. The effect of increasing solar activity on the Sun's total and open magnetic flux during multiple cycles: Implications for solar forcing of climate. Geophysical Research Letters 29, 77–1–77–2. URL: http://doi.wiley.com/10.1029/2002GL015880, doi:10.1029/2002GL015880.

Lenssen, N.J., Schmidt, G.A., Hansen, J.E., Menne, M.J., Persin, A., Ruedy, R., Zyss, D., 2019. Improvements in the gistemp uncertainty model. Journal of Geophysical Research: Atmospheres 124, 6307–6326.

Lévy-Véhel, J., 1998. Introduction to the Multifractal Analysis of Images. Springer Verlag. doi:10.1007/978-3-662-03512-2_17.

Lindzen, R.S., Holton, J.R., 1968. A Theory of the Quasi-Biennial Oscillation. Journal of the Atmospheric Sciences 25, 1095–1107. URL: http://journals.ametsoc.org/doi/10.1175/1520-0469(1968)025{%}3C1095:ATOTQB{%}3E2.0.CO;2, doi:10.1175/1520-0469(1968)025<1095:ATOTQB>2.0.CO;2.

Liou, K.N., Ou, S.C., 1989. The role of cloud microphysical processes in climate: An assessment from a one-dimensional perspective. Journal of Geophysical Research: Atmospheres 94, 8599–8607.

Liu, P.C., 1994. Wavelet spectrum analysis and ocean wind waves, in: Wavelet Analysis and Its Applications. Elsevier. volume 4, pp. 151–166.

Lopes, R., Betrouni, N., 2009. Fractal and multifractal analysis: a review. Medical image analysis 13, 634–649.

Mandelbrot, B.B., Mandelbrot, B.B., 1982. The fractal geometry of nature. volume 1. WH freeman New York.

Maraun, D., Kurths, J., 2004. Cross wavelet analysis: significance testing and pitfalls. Nonlinear Processes in Geophysics 11, 505–514.

Marubashi, K., Cho, K.S., Kim, S., Park, S.H., Ishibashi, H., et al., 2016. The 17 march 2015 storm: the associated magnetic flux rope structure and the storm development. Earth, Planets and Space 68, 173.

Mironova, I.A., Aplin, K.L., Arnold, F., Bazilevskaya, G.A., Harrison, R.G., Krivolutsky, A.A., Nicoll, K.A., Rozanov, E.V., Turunen, E., Usoskin, I.G., 2015. Energetic Particle Influence on the Earth's Atmosphere. doi:10.1007/s11214-015-0185-4.

Morlet, J., Arens, G., Fourgeau, E., Giard, D., 1982a. Wave propagation and sampling theory—Part II: Sampling theory and complex waves. Geophysics 47, 222–236. doi:10.1190/1.1441329.

Morlet, J., Arens, G., Fourgeau, E., Glard, D., 1982b. Wave propagation and sampling theory—Part I: Complex signal and scattering in multilayered media. Geophysics 47, 203–221. doi:10.1190/1.1441328.

Mörner, N.A., 2013. Solar wind, earth's rotation and changes in terrestrial climate. Physical Review & Research International 3, 117–136.

Mukherjee, B., Indira, K., Reddy, R., BV, R.M., 1985. Quasi-biennial oscillation in stratospheric zonal wind and indian summer monsoon. Monthly Weather Review doi:10.1175/1520-0493(1985)113<1421:QBOISZ>2.0.CO;2.

Munnich, M., Cane, M.A., Zebiak, S.E., 1991. A study of self-excited oscillations of the tropical ocean-atmosphere system. J. Atmos. Sci 48, 1238–1248.

Pallé, E., Butler, C., 2002. The proposed connection between clouds and cosmic rays: cloud behaviour during the past 50–120 years. Journal of Atmospheric and Solar-Terrestrial Physics 64, 327–337.

Pallé Bagó, E., Butler, C., 2000. The influence of cosmic rays on terrestrial clouds and global warming. Astronomy & Geophysics 41, 4–18.

Pozo-Vázquez, D., Esteban-Parra, M.J., Rodrigo, F.S., Castro-Díez, Y., 2001. A study of NAO variability and its possible non-linear influences on European surface temperature. Climate Dynamics 17, 701–715. doi:10.1007/s003820000137.

Reed, R.J., 1965a. The present status of the 26-month oscillation. Bulletin of the American Meteorological Society 46, 374–387.

Reed, R.J., 1965b. The quasi-biennial oscillation of the atmosphere between 30 and 50 km over ascension island. Journal of the Atmospheric Sciences 22, 331–333.

Riedi, R.H., 1999. Introduction to multifractals, in: Rice University ECE Technical Report.

Roesch, A., Schmidbauer, H., 2018. Package 'WaveletComp': Computational Wavelet Analysis. URL: https://CRAN.R-project.org/package=WaveletComp. r package version 1.1.

Roesch, A., Schmidbauer, H., Roesch, M.A., 2014. Package 'waveletcomp'. The Comprehensive R Archive Network2014 .

Russell, C., McPherron, R., 1973. Semiannual variation of geomagnetic activity. Journal of geophysical research 78, 92–108.

Schmidbauer, H., Roesch, A., 2018. WaveletComp 1.1: A guided tour through the R package.

Schneider, U., Schönwiese, C.D., 1989. Some starical characteristics of el niño/southern oscillation and north atlantic oscillation indices. Atmosfera 2, 167–180.

Schwartz, R.E., Gershunov, A., Iacobellis, S.F., Cayan, D.R., 2014. North american west coast summer low cloudiness: Broadscale variability associated with sea surface temperature. Geophysical Research Letters 41, 3307–3314.

Sharma, R., Srivastava, N., Chakrabarty, D., Moestl, C., Hu, Q., 2013. Interplanetary and geomagnetic consequences of 5 january 2005 cmes

associated with eruptive filaments. Journal of Geophysical Research: Space Physics 118, 3954–3967.
Sidorenkov, N.S., 2016. Celestial mechanical causes of weather and climate change. Izvestiya - Atmospheric and Ocean Physics 52, 667–682. doi:10.1134/S0001433816070094.
Srivastava, N., 2005a. A logistic regression model for predicting the occurrence of intense geomagnetic storms, in: Annales Geophysicae, pp. 2969–2974.
Srivastava, N., 2005b. Predicting the occurrence of super-storms, in: Annales Geophysicae, pp. 2989–2995.
Srivastava, N., Mathew, S.K., Louis, R.E., Wiegelmann, T., 2009. Source region of the 18 november 2003 coronal mass ejection that led to the strongest magnetic storm of cycle 23. Journal of Geophysical Research: Space Physics 114.
Srivastava, N., Venkatakrishnan, P., 2004. Solar and interplanetary sources of major geomagnetic storms during 1996–2002. Journal of Geophysical Research: Space Physics 109.
Stach, S., Roskosz, S., Cwajna, J., Cybo, J., 2006. Multifractal detection of overlaps based on a stereometric analysis of fracture surfaces: Application to fractures of sintered carbides. Materials Characterization 56, 429–435. URL: https://www.sciencedirect.com/science/article/pii/S1044580306000520, doi:https://doi.org/10.1016/j.matchar.2006.01.007. 9th ECSIA and 7th STERMAT: Stereology and Image Analysis in Materials Science.
Su, C.H., Kiang, J.F., 2022. Effects of sea-surface temperature, cloud vertical structure and wind speed on temperature change between hiatus and post-hiatus periods in tropical western pacific. Atmosphere 13, 2130.
Sun, B., Bradley, R.S., 2002. Solar influences on cosmic rays and cloud formation: A reassessment. Journal of Geophysical Research: Atmospheres 107, AAC–5.
Team, G., 2023. Giss surface temperature analysis (gistemp). NASA Goddard Institute for Space Studies version 4. URL: Datasetaccessed2022-02-20athttps://data.giss.nasa.gov/gistemp/.
Telesca, L., Lapenna, V., Macchiato, M., 2004. Mono-and multi-fractal investigation of scaling properties in temporal patterns of seismic sequences. Chaos, Solitons & Fractals 19, 1–15.
Tiwari, R.K., Pandey, A., Shrivstava, P.K., Srivastava, S.K., 2011. Relationship of cosmic rays with solar and geomagnetic activity. Indian Journal of Scientific Research 2, 15.
Todd, M.C., Kniveton, D.R., 2001. Changes in cloud cover associated with forbush decreases of galactic cosmic rays. Journal of Geophysical Research: Atmospheres 106, 32031–32041.
Torrence, C., Compo, G.P., 1998. A Practical Guide to Wavelet Analysis. Bulletin of the American Meteorological Society 79, 61–78. doi:10.1175/1520-0477(1998)079<0061:APGTWA>2.0.CO;2.
Usoskin, I., Mursula, K., Kangas, J., Gvozdevsky, B., 2001. On-line database of cosmic ray intensities, in: Proceedings of ICRC.
Usoskin, I.G., Kovaltsov, G.A., 2008. Cosmic rays and climate of the Earth: Possible connection. Comptes Rendus - Geoscience 340, 441–450. doi:10.1016/j.crte.2007.11.001.
Véhel, J.L., 2002. Signal enhancement based on hölder regularity analysis, in: Fractals in Multimedia. Springer, pp. 197–209.
Véhel, J.L., Guilheneuf, B., 1997. Multifractal image denoising, in: SCIA'97: 10th Scandinavian conference on image analysis.
Vehel, J.L., Mignot, P., 1994. Multifractal segmentation of images. Fractals 2, 371–377.
Véhel, J.L., Vojak, R., 1995. Multifractal analysis of Choquet capacities: Preliminary results. Ph.D. thesis. INRIA.
Véhel, J.L., Vojak, R., 1998. Multifractal analysis of choquet capacities. Advances in applied mathematics 20, 1–43.
Venkatesan, D., Ananth, A., 1991. Forbush decreases in cosmic rays.
Vines, R., 2008. Australian rainfall patterns and the southern oscillation. 2. a regional perspective in relation to luni-solar (mn) and solar-cycle (sc) signals. The Rangeland Journal 30, 349–359.
Webb, D., Cliver, E., Crooker, N., St Cyr, O., Thompson, B., 2000. Relationship of halo coronal mass ejections, magnetic clouds, and magnetic storms. Journal of Geophysical Research: Space Physics 105, 7491–7508.
Wilson, I.R., 2012. Lunar tides and the long-term variation of the peak latitude anomaly of the summer sub-tropical high pressure ridge over Eastern Australia. Open Atmospheric Science Journal 6, 49–60. doi:10.2174/1874282301206010049.
de Wit, T.D., Watermann, J., 2010. Solar forcing of the terrestrial atmosphere. Comptes Rendus Geoscience 342, 259–272.
Xu, Y., Ji, H., Fermüller, C., 2009. Viewpoint invariant texture description using fractal analysis. International Journal of Computer Vision 83, 85–100.
Yalamova, R., 2006. Wavelet test of multifractality of asia-pacific index price series. Asian Academy of Management Journal of Accounting and Finance 2, 63–83.
Yurchyshyn, V., Tripathi, D., 2010. Relationship between earth-directed solar eruptions and magnetic clouds at 1au: A brief review, in: Advances in Geosciences: Volume 21: Solar Terrestrial (ST). World Scientific, pp. 51–70.
Zeković, A., Reljin, I., 2014. Multifractal analysis of multiview 3d video with different quantization parameters applying histogram method. Serbian journal of electrical engineering 11, 25–34.